ACS NANO

www.acsnano.org

ARTICLE

Nanomechanical Sensing for Mass Flow Control in Nanowire-Based Open Nanofluidic Systems

Javier E. Escobar,[‡] Juan Molina,[‡] Eduardo Gil-Santos, José J. Ruz, Óscar Malvar, Priscila M. Kosaka, Javier Tamayo, Álvaro San Paulo,* and Montserrat Calleja

Cite This: *ACS Nano* 2023, 17, 21044−21055

Read Online

ACCESS | Metrics & More | Article Recommendations | Supporting Information

ABSTRACT: **Open nanofluidic systems, where liquids flow along the outer surface of nanoscale structures, provide otherwise unfeasible capabilities for extremely miniaturized liquid handling applications. A critical step toward fully functional applications is to obtain quantitative mass flow control. We demonstrate the application of nanomechanical sensing for this purpose by integrating voltage-driven liquid flow along nanowire open channels with mass detection based on flexural resonators. This approach is validated by assembling the nanowires with microcantilever resonators, enabling high-precision control of larger flows, and by using the nanowires as resonators themselves, allowing extremely small liquid volume handling. Both implementations are demonstrated by characterizing voltage-driven flow of ionic liquids along the surface of the nanowires. We find a voltage range where mass flow rate follows a nonlinear monotonic increase, establishing a steady flow regime for which we show mass flow control at rates from below 1 ag/s to above 100 fg/s and precise liquid handling down to the zeptoliter scale. The observed behavior of mass flow rate is consistent with a voltage-induced transition from static wetting to dynamic spreading as the mechanism underlying liquid transport along the nanowires.**

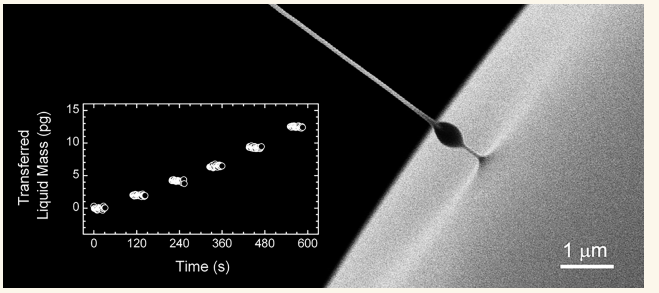

KEYWORDS: *semiconductor nanowires, silicon nanowires, nanoelectromechanical systems (NEMS), nanomechanical resonators, nanofluidics, open fluidics, ionic liquids*

Recent research in nanofluidics has led to exciting results regarding both scientific breakthroughs and emerging technologies.[1] The control of liquid transport through extremely miniaturized enclosing nanostructures, including nanopores,[2−4] nanotubes,[5−7] or nanoslits,[8,9] has enabled the exploration of intriguing properties such as anomalous ordering and dielectric behavior in nanoconfined water,[8,10] enhanced water flow in carbon channels[2,6−8] or Coulombic effects in liquid transport,[3,11] as well as establishing the basis for efficient technologies for ion separation[2,7,12,13] or osmotic energy conversion.[4,5,14] In addition to closed systems, where fluids are bounded by solid structures, open fluidic systems, in which liquids move along the surface of exposed channels, provide an alternative approach with complementary features,[15−17] often inspired in biomaterials.[18,19] In open systems, liquids flow either partially enclosed along the sidewalls of wedges or grooves,[15,20,21] suspended between guiding rails,[22−24] or totally exposed along the outer surface of free-standing structures such as cones or fibers,[25−28] providing simplified fabrication, reliable operation, ease of surface modification, exceptionally large liquid/channel volume ratios and exposure of the liquid−gas interface for liquid input/sampling. The use of high aspect ratio nanostructures based on nanowires or nanotubes for driven flow of liquids along their external surface has led the way toward functional open nanofluidics.[29−31] These nanostructures promise highly localized and precise interactions with biological analytes and interfaces, consisting, for instance, in fluid delivery/retrieval, bioassays, or analyte transfer/extraction/tracking.[16,32,33]

Flow control, comprising driven liquid transport and flow rate sensing, is a critical issue in the miniaturization of fluidic technologies.[34] Diverse approaches have been explored for

Received: May 5, 2023
Revised: October 16, 2023
Accepted: October 19, 2023
Published: October 30, 2023

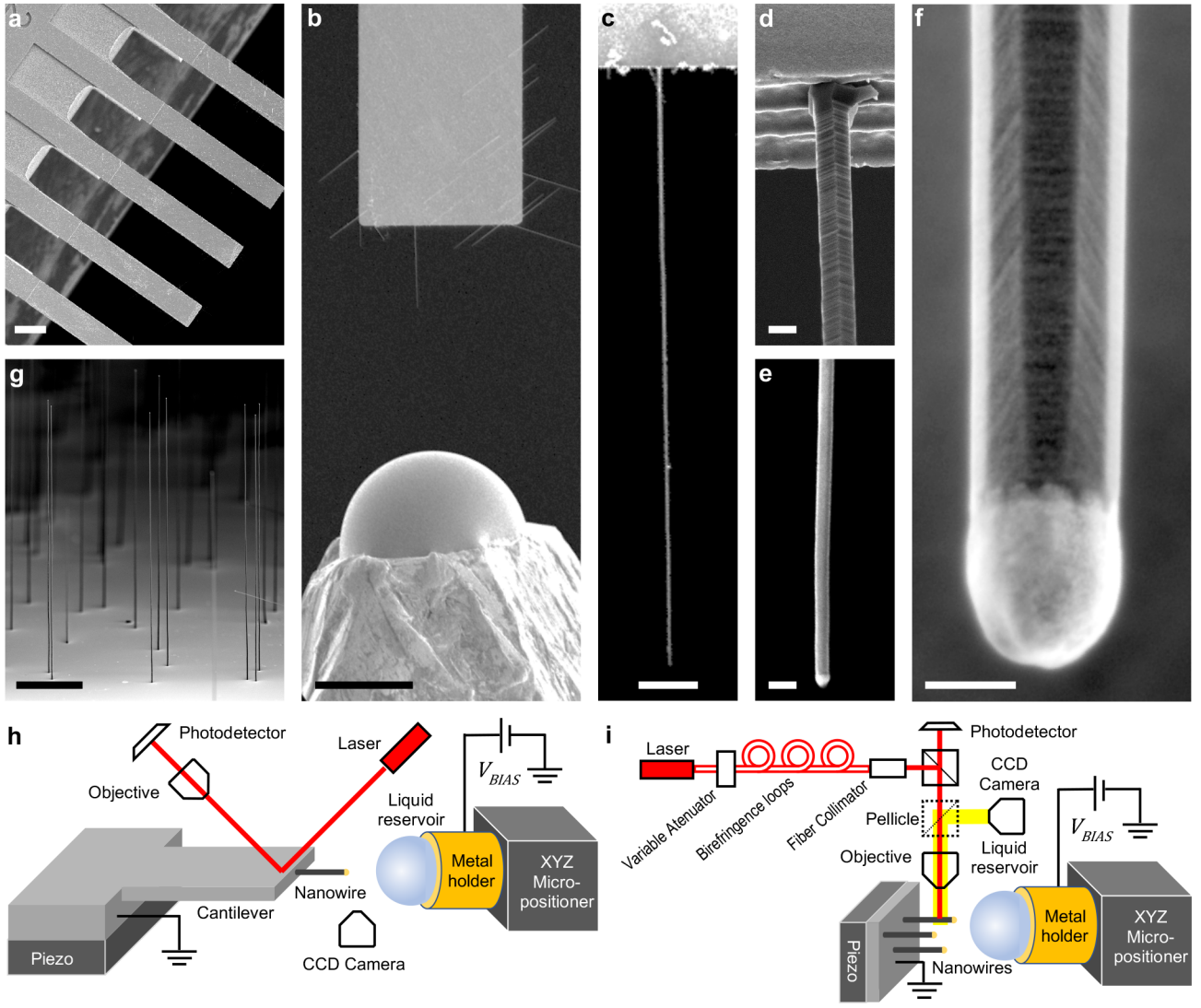

Figure 1. Devices and instrumental setups. (a) SEM image of an array of Si cantilevers with their longitudinal axis aligned along a (111) direction used for the fabrication of MCNW devices (scale bar 100 μm). (b) MCNW device positioned in proximity of an IL (IL1) microdroplet reservoir placed on a metal support (scale bar 50 μm). (c) Full length of a NW grown at the edge of a cantilever (scale bar 5 μm). (d) Epitaxial NW clamp at the cantilever edge (scale bar 200 nm). (e) Free NW end (scale bar 200 nm). (f) VLS growth remaining NP at the NW tip (scale bar 100 nm). (g) Si NWs grown on a plain substrate as those used as SANW devices (scale bar 10 μm). (h) Schematic representation of the measurement setup for the MCNW devices, based on laser-beam deflection transduction. (i) Schematic representation of the measurement setup for the SANW devices, based on laser-beam scattering modulation transduction.

closed nanofluidic systems,[6,35,36] and driven liquid transport has been demonstrated in open systems by a variety of methods, including built-in capillary/wettability forces[19,25−27] or external electrical actuation.[28−31,37] Quantitative control of liquid transport in open systems is currently limited by the difficulty to obtain precise flow rate sensing. Flow rate measurements are mostly based so far on the estimation, by imaging methods, of changes of liquid volumes acting as initial reservoirs or being involved in the transport.[27,30,31,38] Besides limitations in accuracy, these estimations are impractical for the development of compact integrated systems that fully exploit the potential of open nanofluidics. In this work we demonstrate the integration of electrically driven liquid transport with nanomechanical flow rate sensing for mass flow control in open nanofluidic systems. Nanomechanics has been fruitfully combined before with fluidic technologies in a variety of contexts, from buoyant mass detection of bioanalytes[39−41] to ultralow volume liquid handling[42−44] or surface wettability and evaporation dynamics research.[45,46] Our approach for mass flow control relies on the combination of free-standing open nanofluidic channels with frequency shift tracking of the flexural resonances of beam resonators that integrate these channels. We prove this approach by two complementary implementations: In one, nanowire (NW) open channels are assembled with microcantilever (MC) resonators so that each component provides separate functionality, either liquid transport or mass sensing, respectively; in another, NWs operate simultaneously as open channels and flexural resonators, providing dual functionality. The microcantilever-nanowire (MCNW) devices allow larger volume handling given the much larger mass of the MC resonators as compared to the NWs, whereas the stand-

https://doi.org/10.1021/acsnano.3c04020
ACS Nano 2023, 17, 21044−21055

alone nanowire (SANW) approach optimizes mass resolution, enabling extremely small liquid volume control.

Liquids can evolve along the outer surface of high aspect ratio structures as a thin precursor film or as beads.[47] This behavior has been observed at the nanoscale for ionic liquids (ILs) transferred to semiconductor NWs[29] and aqueous solutions spreading along carbon nanotube based fibers[30,31] under the effect of direct current (dc)[29,30] and alternating current (ac)[31] driving voltages. However, a precise control of the liquid traveling along this type of nanostructures has not been possible so far, mostly due to the lack of adequate methods to measure the resulting flow. Our mass flow control approach combines highly precise driving and sensing of liquids traveling along this type of systems by integrating nanomechanical liquid mass detection with dc voltage driven flow. We demonstrate this approach by characterizing the flow of ILs along the surface of Si NWs when a bias dc voltage is applied between the NWs and a microscopic IL reservoir droplet where the NWs are partially immersed. ILs are fluids composed of ions rather than molecules, i.e., molten salts at room temperature, that have many singular and useful features such as high thermal/chemical stability and negligible vapor pressure.[48] These fluids are of great potential interest for open nanofluidics given their widely tunable properties with regard to polarity, hydrophobicity, miscibility, and solvation, and they are the subject of research for multiple bioapplications such as biocatalytic reactions, protein stabilization, and biopreservation.[49−51] In the context of this work, the extremely low vapor pressure of ILs makes evaporation losses negligible even in vacuum,[52] ensuring that all measured mass changes can be attributed to transport between the reservoir and the NWs. Our results reveal a voltage range where ILs can be made to flow along NWs with precise control. The characterization of flow rate vs voltage points out to voltage-induced variation of the solid/liquid interfacial tension between the NW and the IL as the mechanism governing liquid transport, analogously to electrowetting. We also describe different operation modes that allow to either accumulate relatively large amounts of liquid on the NWs or to iterate small volume liquid exchanges with the reservoir, suggesting diverse types of applications. Finally, we show how the high mass resolution of the SANW devices enables the capability of handling extremely small volumes of liquid, providing a quantitative tool to characterize fundamental wetting/spreading properties of liquids at the nanoscale with high sensitivity.

RESULTS AND DISCUSSION

Device Fabrication, Experimental Setup, and Measurement Methodology. Figure 1 describes the fabricated devices and the experimental setups. Si NWs were obtained by vapor−liquid−solid (VLS) growth[53] with lengths in the range of 40−50 μm, base diameters of 200−400 nm and tip diameters of 50−250 nm. MCNW devices are composed of a Si MC with a Si NW grown at the free end in parallel to the longitudinal axis (Figures 1a−c).[54−56] The MCs have a nominal length of 500 μm, width of 90 μm, and thickness of 1 μm. A solid and continuous clamp of the NW to the MC is provided by the epitaxial growth mechanism (Figure 1d).[57] NW tapering is expected to favor liquid flow from the tip toward the base (Figures 1d,e),[18,25] and it also enhances mass sensitivity.[58,59] The cross-section at the base is hexagonal with a roughly regular section and a sawtooth surface corrugation (Figure 1d). This morphology evolves along the NW so that for the last few micrometers near the tip the facet edges and the surface corrugation are significantly smoothed (Figures 1e,f). The growth process generates gold−silicon oxide core−shell nanostructures that remain at the tip of the NWs (Figure 1f).[53] The SANW devices consist of Si NWs vertically grown on raw Si (111) substrates (Figure 1g).[60] The use of long NWs provides ample liquid capacity for testing MCNW devices, and it allows to confine liquid transport to the very last section of the NWs near the tip in the case of SANW devices.

Liquid flow measurements were performed by resonance frequency tracking before and after partial immersions of the Si NWs in an IL reservoir droplet. The immersions were performed by a custom fabricated stage where the IL reservoir droplet is placed on a conductive support moved by a software-controlled *XYZ* micropositioner (Figure 1b). During the immersion time, a dc bias voltage can be applied between the IL conductive support and the devices in order to drive liquid flow from the droplet to the NWs.[29] The immersion stage is modular, so that it can be operated within a SEM in high vacuum conditions (10^{-7} mbar). This allowed for imaging NW immersions into the IL droplet in order to check the procedure control. We used two particular ILs: DMPI-TFSI (IL1) and DEME-TFSI (IL2). IL1 has been previously used in open nanofluidics research involving NWs.[29] IL2 has similar properties to IL1 (Supporting Information, section 1), but it has better commercial availability and offers a slightly wider electrochemical window.[61,62] The two ILs have provided indistinguishable results in this work. Resonance frequency tracking was performed by optical readout (see the "Methods" section), either using laser beam deflection for MCNW devices (Figure 1h)[63] or scattering modulation for SANW devices (Figure 1i).[59] In order to demonstrate our approach in relevant experimental conditions, MCNW devices were operated in air, consistently with most common practical situations; complementarily, SANW operation was performed in vacuum (10^{-5} mbar), aiming to explore the resolution limits of the approach, which benefits from quality factor optimization in such conditions.

The fundamental resonance frequency f_R and quality factor Q of the MCs are in the range of 6−12 kHz and 10−40, whereas for the NWs they take values around 200−300 kHz and 10,000−20,000, respectively. Frequency stability (Allan deviation, $\delta f_{NOISE}/f_R$), for both types of devices is in the range of 0.1−1 ppm for acquisition times between 1 and 100 s. The mass of liquid transferred from the reservoir to the NWs is estimated from the point-mass approximation as $\Delta m = -2m_R \cdot \Delta f_R/f_R$, where m_R is the effective mass of the resonator and Δf_R is the measured resonance shift.[64] A correction on the effective mass of the MC that accounts for the effect of mass adsorption at the end of the NW assembled at the MC free end needs to be made in order to optimize the accuracy of mass measurements (Supporting Information, section 2). In addition, the error of the point-mass approximation increases as the liquid moves from the tip to the base of the NWs. A given percentage of the relative extension of the liquid from the NW tip with respect to the total resonator length implies a comparable relative error in the estimation of the liquid mass (Supporting Information, section 3). In consequence, we use our flow control approach to constrain IL transport near the free end of the resonators, typically below a 5% of their total length. This implies a maximum distance from the tip of the NWs of around 25 μm for MCNW devices and 2 μm for SANW devices. Under the same approximation, the exper-

https://doi.org/10.1021/acsnano.3c04020
ACS Nano 2023, 17, 21044−21055

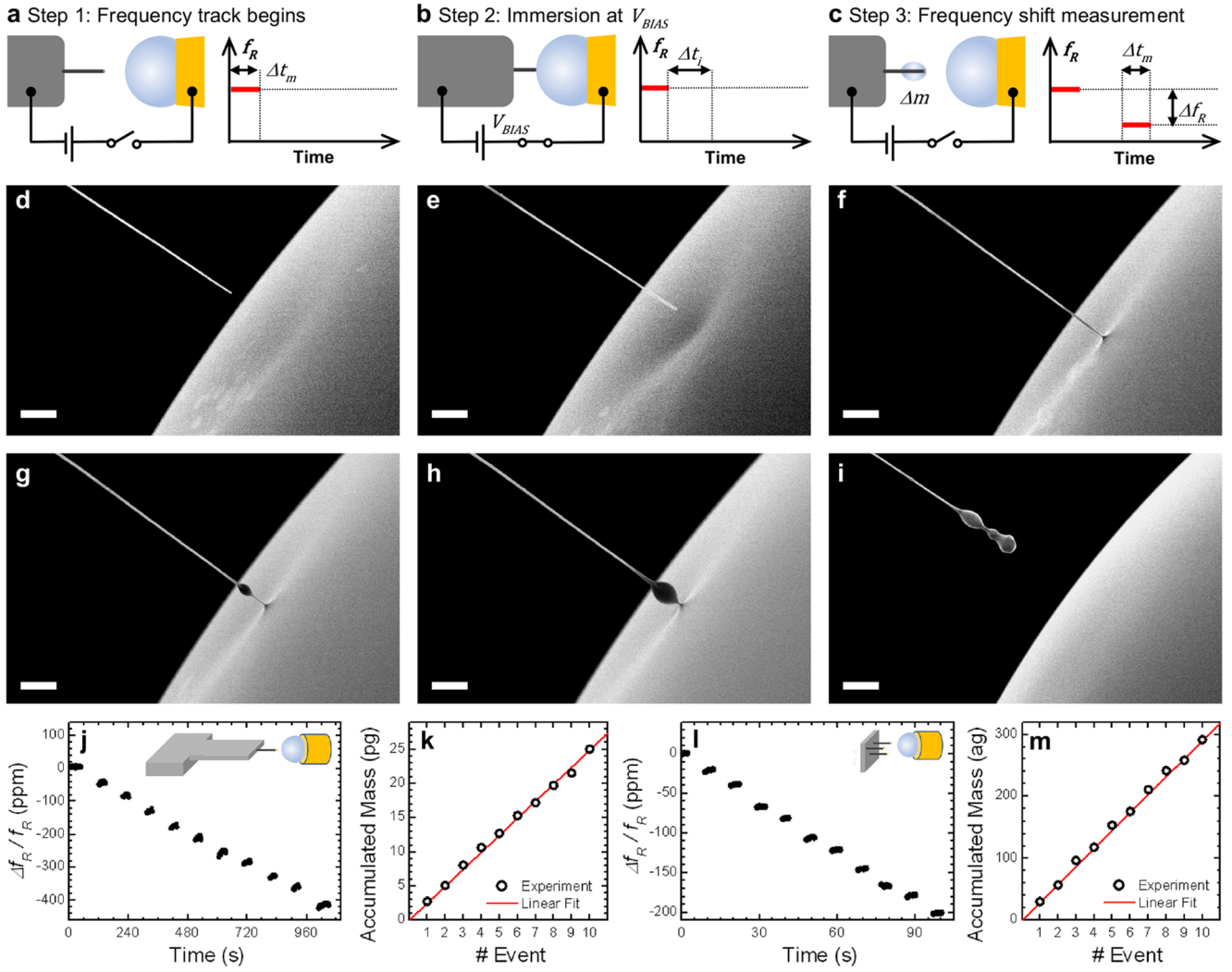

Figure 2. Experimental methodology. (a–c) Schematic description of the measurement procedure: Step 1, resonance frequency measurement before NW immersion into an IL reservoir droplet (a); Step 2, partial immersion of the free NW end for a controlled immersion time and bias voltage (b); Step 3, NW withdrawal and resonance frequency shift measurement after NW immersion (c). (d–i) Sequence of SEM images acquired during the immersion of a NW into an IL (IL1) reservoir droplet for a bias voltage of 2.5 V and an immersion time of 9 min, showing the driven flow of IL to the NW (scale bars 1 μm), and representative of the steps described above (step 1: d, e; step 2: f, g, h; step 3: i). (j) Example of resonance frequency tracking during a series of 10 iterated immersions of 60 s into an IL2 reservoir in air with a bias voltage of 2.8 V for a MCNW device, showing the clear frequency downshifts after each immersion (for clarity, data is shown only during the measurement intervals between consecutive immersions). (k) Linear mass accumulation on the NW after each immersion event of the series plotted in (j). (l) Example of resonance frequency tracking during a series of 10 iterated immersions of 5 s into an IL1 reservoir in high vacuum with a bias voltage of −1.4 V for a SANW device, showing also clear frequency shifts. (m) Linear mass accumulation on the NW after each immersion event of the series plotted in (l).

imental mass detection limit can be estimated from frequency stability measurements as $\delta m = -2m_R \cdot \delta f_{NOISE}/f_R$, resulting in the range of 10–100 fg for the MCNW devices and 0.1–1 ag for the SANW devices, depending on the exact dimensions and noise performance of each particular device.[59]

Figure 2 describes our experimental methodology. IL transfer from the reservoir to the NWs follows three steps: 1) Before partial NW immersion into the droplet, the resonance frequency of the fundamental flexural mode of the resonator is measured for a time interval Δt_m while keeping the NW separated from the droplet with no bias voltage applied (Figure 2a). 2) IL flow from the droplet to the NW is generated by immersion of a portion of around 0.5 μm of the NW into the droplet for a time Δt_i during which a bias voltage V_{BIAS} can be applied in order to drive the flow (Figure 2b). 3) The IL mass Δm transferred to the NW produces a downshift Δf_R in the resonance frequency of the resonator which is determined from the measurement of the resonance frequency after immersion, setting a new reference for a subsequent immersion (Figure 2c). Then, the mass flow rate $\dot{m}$ can be determined as $\dot{m} = \Delta m/\Delta t_i$. Figures 2d–i show a partial immersion of a NW into an IL reservoir droplet and the transfer of IL from the droplet to the NW. The immersion time was particularly long (9 min) in order to transfer a sufficiently large amount of IL to be clearly observed by the SEM. The change in image contrast at the last section of the NW right upon immersion (Figure 2f) suggests the formation of an IL precursor film on the NW.[29] At longer times, the formation of liquid beads on the NW is usually observed (Figure 2g), the size of which increases as IL continues to flow (Figure 2h).

https://doi.org/10.1021/acsnano.3c04020
ACS Nano 2023, 17, 21044–21055

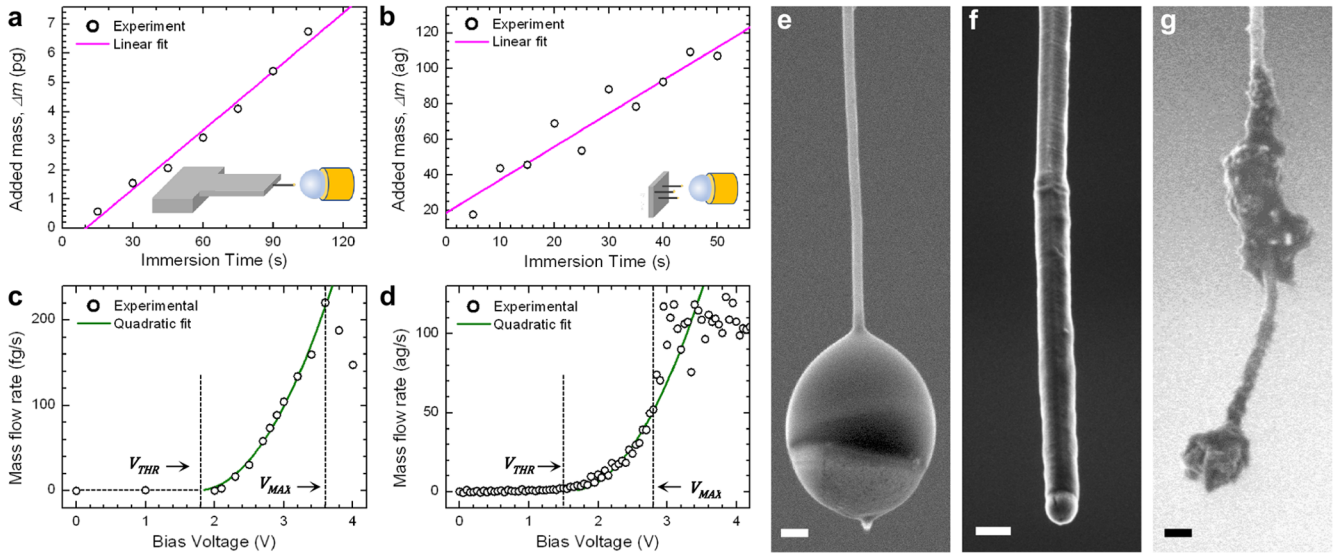

Figure 3. Characterization of mass flow control performance. (a) Linear behavior of added mass per immersion as a function of immersion time for a fixed bias voltage (2.7 V) for a MCNW device and an IL2 reservoir. (b) Linear behavior of added mass per immersion as a function of immersion time for a fixed voltage (2.2 V) for a SANW device and an IL1 reservoir. (c) Functional regimes and nonlinear behavior of mass flow rate vs bias voltage, represented for a fixed immersion time (60 s) for a MCNW device and an IL2 reservoir. (d) Functional regimes and nonlinear behavior of mass flow rate vs bias voltage, represented for a fixed immersion time (5 s) for a SANW device and an IL1 reservoir. (e, f) SEM images of the free end of the NW of a MCNW (e) and a SANW device (f) after operation within the flow regime (scale bars 200 nm). (g) SEM image of the end of the NW of a MCNW device after operation above the onset of electrochemical processes (scale bar 200 nm).

Table 1. Experimental Parameters and Results of Mass Flow Control Experiments

MCNW devices (air)										
device no.	f_R (kHz)	Q	δm (fg)	L (μm)	D_{BASE} (nm)	D_{TIP} (nm)	V_{THR} (V)	V_{MAX} (V)	$\dot{m}_{MIN}$ (fg/s)	$\dot{m}_{MAX}$ (fg/s)
1	6.169	17	85	45.2	294	57	2.0	2.8	1.4	86
2[a]	9.009	28	18	40.7	362	61	16	42	16	147
3[a]	8.730	32	15	44.5	300	122	5.0	30	8.2	50
4	11.99	35	25	42.8	331	121	1.8	3.6	0.4	216
5	7.642	23	54	43.7	455	255	2.0	3.0	0.9	563
SANW devices (vacuum)										
device no.	f_R (kHz)	Q	δm (ag)	L (μm)	D_{BASE} (nm)	D_{TIP} (nm)	V_{THR} (V)	V_{MAX} (V)	$\dot{m}_{MIN}$ (ag/s)	$\dot{m}_{MAX}$ (ag/s)
1	312.4	18,000	0.15	33.0	220	88	2.1	2.9	0.3	38
2	211.2	8,000	0.36	41.8	254	87	1.5	2.8	1.1	52
3[a]	237.3	19,000	0.48	48.3	384	177	1.4	2.8	2.6	156
4[a]	269.6	12,000	0.43	40.0	320	178	0.9	1.7	3.5	256
5[a]	231.3	12,000	0.96	44.1	315	166	1.1	1.9	2.6	298

[a]Negative biasing; f_R, device resonant frequency; Q, device quality factor; δm, experimental mass detection limit; L, NW length; D_{BASE}, NW base diameter; D_{TIP}, NW tip diameter; V_{THR}, threshold voltage for steady flow (abs. value); V_{MAX}, maximum voltage below electrochemical regime (abs. value); $\dot{m}_{MIN}$, minimum mass flow rate; $\dot{m}_{MAX}$, maximum mass flow rate.

When removing the NW from the reservoir, the beads can remain in place or split into several smaller ones (Figure 2i). This has a negligible effect on the mass measurements as the total mass remains near the NW free end. Representative examples of resonance frequency tracking measurements during IL transfer experiments for a MCNW and a SANW device are shown respectively in Figure 2j,l. The resulting determination of the added mass linearly accumulated on the NWs is presented in Figures 2k,m. The mass transferred for each immersion event is obtained from the frequency shift corresponding to the difference between each step. The total mass accumulated on the NWs follows a linear trend, indicating that the mass transferred in each immersion event is approximately constant for a given immersion time and voltage. In these examples, the mass transferred per immersion takes average values of 2.49 ± 0.03 pg and 29.5 ± 0.3 ag respectively for the MCNW and the SANW devices. These values imply mass flow rates of 42 fg/s and 5.8 ag/s for each experiment.

Characterization of Mass Flow Control Performance. Two parameters can modulate the IL mass transfer from the reservoir to the NWs: the immersion time and the bias voltage. In Figure 3 we show representative examples of the analysis of the effects of these two parameters on the IL flow for both a MCNW and a SANW device. Figure 3a shows a measurement of the IL mass transferred per immersion event as a function of the immersion time as measured with a MCNW device for V_{BIAS} = 2.7 V. The immersion time increases from 15 to 105 s,

https://doi.org/10.1021/acsnano.3c04020
ACS Nano 2023, 17, 21044−21055

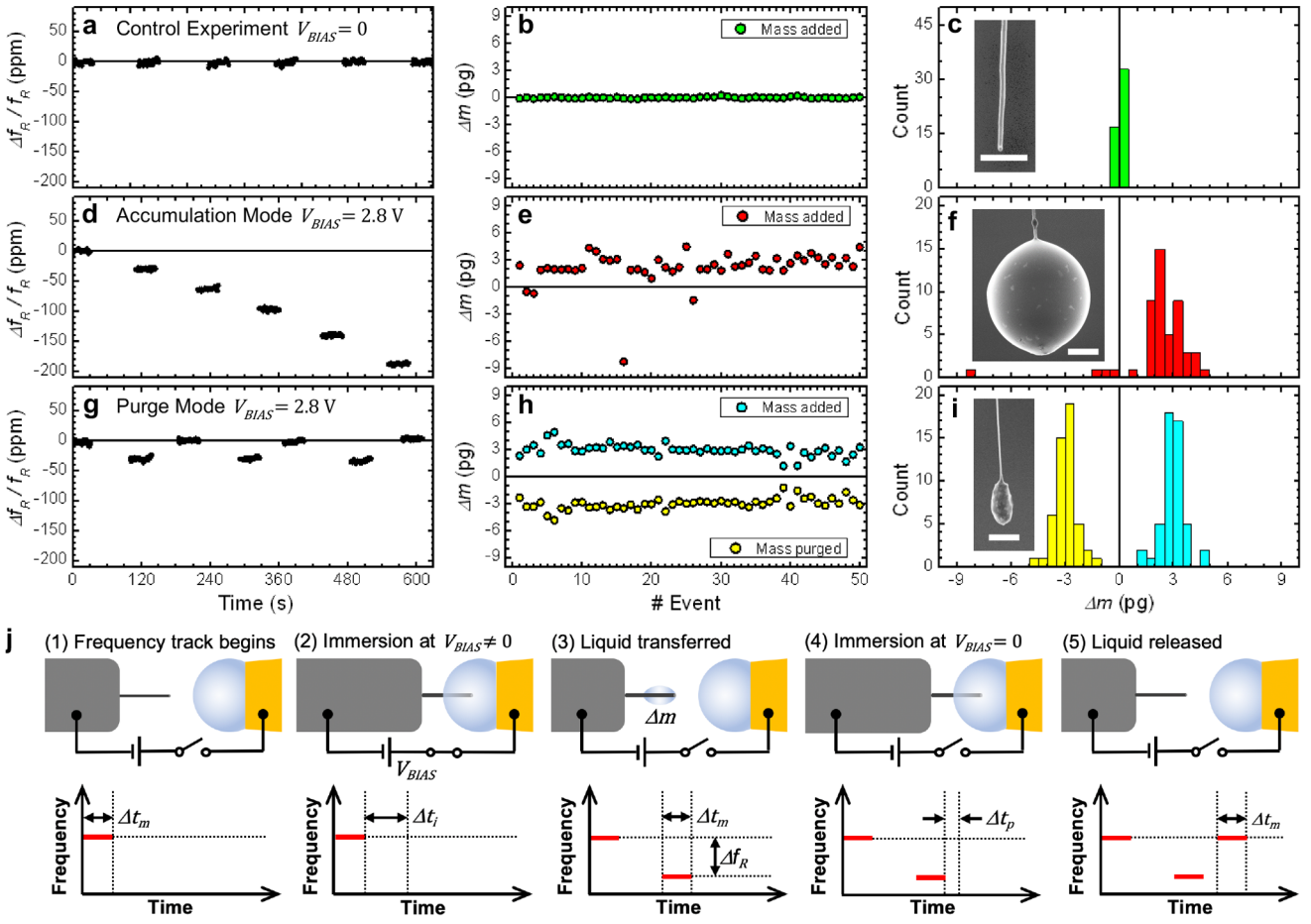

Figure 4. Liquid mass transfer performance in different operation modes. (a) Resonance frequency track during 5 consecutive immersions of 60 s at V_{BIAS} = 0. (b) Mass of IL transferred per immersion event for 50 consecutive immersions of 60 s for V_{BIAS} = 0. (c) Histogram of the data represented in (b); Inset: SEM image of the NW free end after the control experiment (scale bar 1 μm). (d) Resonance frequency track during 5 consecutive immersions of 60 s at V_{BIAS} = 2.8 V in accumulation mode. (e) Mass of IL transferred per immersion event in accumulation mode for 50 consecutive immersions of 60 s for V_{BIAS} = 2.8 V. (f) Histogram of the data represented in (e); Inset: SEM image of the NW free end after the experiment in accumulation mode (scale bar 2 μm). (g) Resonance frequency track during 3 consecutive immersions of 60 s at V_{BIAS} = 2.8 V in purge mode. (h) Mass of IL transferred and released per immersion cycle in purge mode for 50 consecutive cycles with immersion and purge times of 60 and 30 s, respectively, and for V_{BIAS} = 2.8 V. (i) Histograms of the added/purged mass data represented in (h); Inset: SEM image of the NW free end after the experiment in purge mode (scale bar 2 μm). (j) Schematic depiction of the steps followed in purge mode. All experiments were performed with a MCNW device and an IL2 reservoir.

which results in a linear increase of the mass transferred per immersion from 0.6 to 6.8 pg. This linear increase implies that during each immersion, the liquid mass transfer happens at a uniform rate over time. The flow rate reaches a value of 67 ± 4 fg/s for this example. An equivalent linear behavior is obtained for SANW devices, as shown in Figure 3b for a device biased at V_{BIAS} = 2.2 V. In this case, immersion times from 5 to 50 s produce a lower mass transfer, in the range of 20−110 ag, corresponding to a flow rate of 1.9 ± 0.2 ag/s. The effect of the applied bias voltage on the flow rate is shown in Figure 3c with an example for a MCNW device (Δt_i = 60 s) and in Figure 3d for a SANW device (Δt_i = 5 s). A similar behavior is observed in both cases: Below a given threshold voltage V_{THR}, no mass flow is detected by either device; between V_{THR} and a maximum voltage V_{MAX}, the mass flow rate rises monotonically following a nonlinear increase that fits well to a quadratic trend, establishing a steady flow regime; finally, above V_{MAX}, the mass flow rate stops increasing, and does not follow a well-defined behavior. Figure 3e,f shows representative SEM images of NWs after mass transfer experiments with MCNW and SANW devices, respectively. Larger amounts of liquid typically result in the formation of beads, whereas smaller amounts remain as films. The estimation of added mass from the volumes measured in the SEM images agrees with the mass determined from frequency shift measurements (Supporting Information, section 4).

The behavior of mass flow rate vs voltage described above has been qualitatively reproduced by different devices regardless of ambient conditions and biasing polarity. Table 1 presents a summary of the results from 10 different measurements of mass flow rate vs voltage, each done with a different device for positive or negative bias voltage. The data for MCNW device 4 and SANW device 2 corresponds to Figure 3c,d, respectively. Equivalent results were obtained in terms of flow direction regardless of the bias voltage polarity: Liquid transport from the reservoir to the NWs was observed for both positive and negative biasing. The steady flow regime is observed at a few volts, with slight deviations in V_{THR} and V_{MAX} among devices attributed to small variations in their electrical properties. Singularly, the steady flow regime for

https://doi.org/10.1021/acsnano.3c04020
ACS Nano 2023, 17, 21044−21055

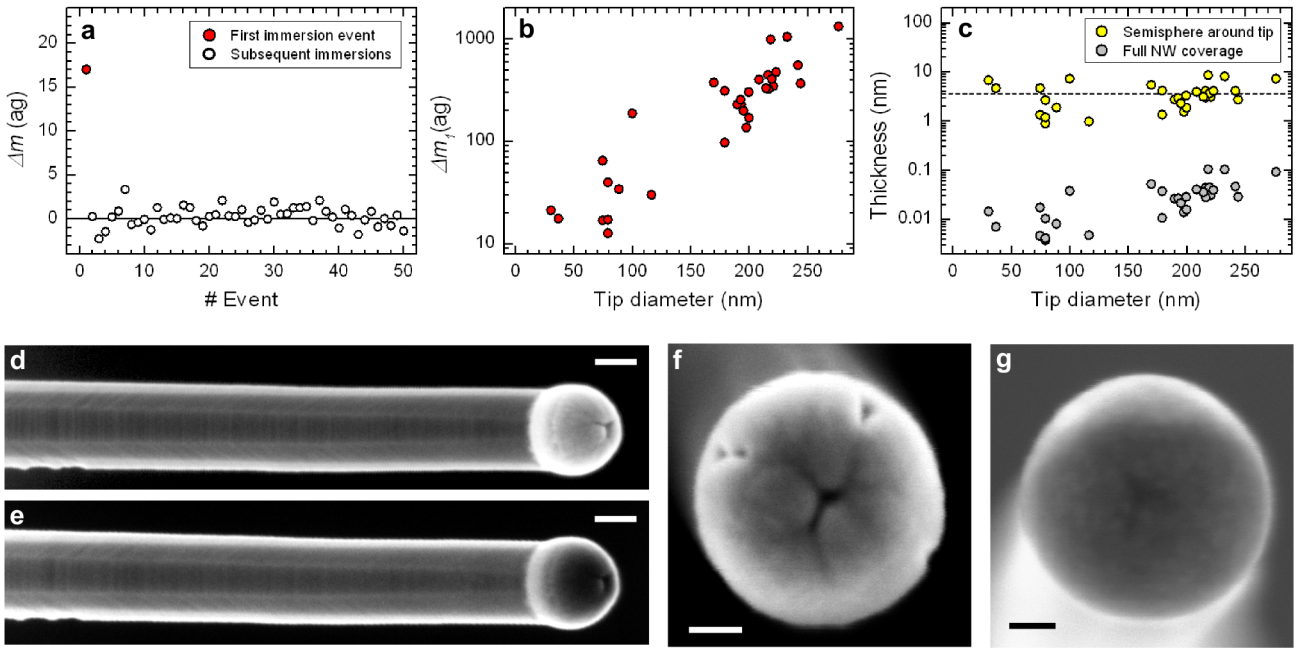

Figure 5. High-resolution measurements of liquid transfer at zero bias voltage. (a) Added mass per immersion event at zero bias voltage measured with a SANW device during a single experiment with IL2. (b) Added mass for the first immersion event for $N = 32$ experiments with different NWs as a function of the NW tip diameter. (c) Estimation of the thickness of an IL film covering only the nanoparticle at the end of the NWs assuming a semispherical shell shape or covering the full NW length. (d, e) SEM images of a Si NW before (d) and after (e) iterative immersions at zero bias voltage (scale bars 100 nm). (f, g) SEM images of the tip of NWs (top view) before (f) and after (g) iterative immersions at zero bias voltage (scale bars 50 nm).

negative biasing in air was observed at higher voltages, around a few tens of volts. The range of operation for mass flow control can be obtained from each measurement by determining the minimum and maximum mass flow rates, $\dot{m}_{MIN}$ and $\dot{m}_{MAX}$, respectively, that set the limits of the steady flow regime. The values of $\dot{m}_{MIN}$ and $\dot{m}_{MAX}$ presented in Table 1 were obtained by fitting the data to a function $\dot{m} = \dot{m}(V)$ that is quadratic within the steady flow regime (see "Methods" section), so that $\dot{m}_{MIN} = \dot{m}(V_{THR})$ and $\dot{m}_{MAX} = \dot{m}(V_{MAX})$. The particular flow rate values achieved in each case depend on several factors. For instance, larger diameter NWs tend to provide larger flow rates. Also, larger flow rates were systematically obtained with MCNW devices in air as compared to SANW devices in vacuum. This points out to a strong influence of the ambient conditions on the IL fluidity at the nanoscale. Notably, these results demonstrate a range of mass flow control of up to 2 orders of magnitude for individual devices, and an overall range for all measurements that spans 6 orders of magnitude.

The observation of a threshold voltage for triggering driven liquid flow is consistent with a transition from a static wetting to a dynamic spreading regime.[47] The evolution of liquids on solid surfaces is described by the spreading parameter $S = \gamma_{SV} - \gamma_{SL} - \gamma_{LV}$, where γ_{SV} is the solid/vacuum (or vapor) interfacial tension, γ_{SL} is the solid/liquid one, and γ_{LV} is the interfacial tension between liquid and vacuum (or vapor).[65] The sign of S determines the behavior of the liquid: For $S < 0$, the liquid partially wets the surface statically with a contact angle θ given by the Young's equation: $\cos\theta = 1 + S/\gamma_{LV}$; for $S \geq 0$ the liquid spreads out and forms a thin film on the solid. The effect of voltage application between the NW and the liquid reservoir is provided by Lippmann's equation: $\gamma'_{SL} = \gamma_{SL} - \frac{1}{2}CV^2$, where γ'_{SL} is the voltage dependent interfacial tension between solid and liquid and C is the interface capacitance per unit area.[66] Thus, a voltage dependent spreading parameter S' can be written as $S' = \frac{1}{2}C(V^2 - V_{THR}^2)$, where the threshold voltage V_{THR} is given by $V_{THR} = \left|\frac{2S}{C}\right|^{1/2}$. Then, the spreading transition occurs for $V \geq V_{THR}$, so that the liquid evolves from a static meniscus at the NW tip to developing a microscopic film that spreads along the NW. The presence of a threshold voltage and a nonlinear response of mass flow rate in the steady flow regime, resulting from the quadratic dependence of γ'_{SL} on the voltage, evidence a liquid transport mechanism governed by the voltage-induced variation of γ'_{SL}, the same mechanism underlying electrowetting.[66] The singular behavior of mass flow rate for negative biasing in air is indeed consistent with previously reported electrowetting behavior of ILs.[67] The observation of much larger flow rates in air as compared to vacuum is coherent with the expected effects of ambient conditions on the fluidity of ILs by means of their capacity to adsorb significant amounts of water from the atmosphere,[68,69] which is known to result in extreme alterations of their viscosity.[70,71] In addition, nanoscale confinement and low dimensionality are also expected to further influence the effects of ambient conditions on IL fluidity.[72] On the other hand, the observation of a maximum voltage is related to the onset of electrochemical processes, which has been reported to occur close to the typical values we obtain for V_{MAX} for the ILs under test.[61,62] SEM images of NWs after operation above V_{MAX} (Figure 3g) often show clear signs of morphological alterations that we attribute to electrochemical processes. Further discussion about the influence of bias polarity and ambient conditions on the mass flow rate behavior is provided in section 5 of the Supporting Information.

https://doi.org/10.1021/acsnano.3c04020
ACS Nano 2023, 17, 21044−21055

Operation Modes. The methodology presented above allows the implementation of different operation modes. Two examples are shown in Figure 4 for a MCNW device. The larger amount of liquid that this type of devices can handle allows for a better comparison of these modes. Figure 4a−c represent a control experiment in which 50 immersions are carried out iteratively at zero bias voltage for Δt_i = 60 s. The resulting mass transferred per immersion has a negligible average value. Consistently, no traces of liquid are evident along the NW by SEM imaging after the experiment (inset in Figure 4c). In Figure 4d−f we present the termed "accumulation mode". Here, immersion events are iterated just as described in Figure 2, so the liquid transferred during each immersion event accrues on the NW for the next immersion. For the conditions of the experiment (V_{BIAS} = 2.8 V and Δt_i = 60 s), the average mass transferred per event is 2.2 ± 1.9 pg, and the mass accumulated after 50 immersions reaches 111 pg. This mass forms an approximately spheroidal droplet of liquid at the NW free end, as shown in the SEM image (inset in Figure 4f).

We have devised a different procedure, termed "purge mode", in which an arbitrarily large number of immersions can be performed while keeping a limited accumulated mass. In the purge mode, every single immersion step and its subsequent frequency measurement step are followed by a liquid release step. This release step consists of quick and short immersions in close succession (rate ∼ 1 Hz) of the NW into the reservoir at zero bias voltage for a time Δt_p and with an immersion depth larger (∼20 μm) than that used for the IL transfer step (Figure 4j). After the release step, the resonance frequency recovers to a value very close to the initial one, which means that most of the liquid is transferred back from the NW to the reservoir. Thus, even after a large number of mass transfer-release iterations, the mass accumulated on the NW remains typically smaller than the mass transferred in a single event. An example is presented in Figure 4g−i. In this case (V_{BIAS} = 2.8 V, Δt_i = 60 s and Δt_p = 30 s), the average mass transferred per event is 3.0 ± 0.7 pg, a value comparable to that obtained in accumulation mode for the same parameters. However, the mass remaining on the NW after the 50 transfer-release iterations reaches only 0.9 pg. This measurement is consistent with the SEM image (inset in Figure 4i), which shows a small residual mass at the NW tip. One significant observation from the results presented in Figure 4 is that whereas the dispersion of the measurements of mass transferred per immersion event for the control experiment at zero bias voltage is comparable to the mass detection limit of the device (so that dispersion can be attributed to frequency noise), the mass dispersion in both the accumulation and purge mode experiments at nonzero bias voltage is around 1 order of magnitude higher, so that it is interpreted as dispersion in the amount of liquid transferred per immersion event.

High-Resolution Measurements. SANW devices provide the chance to exploit the lower limits of mass resolution for extremely small liquid volume control. A representative example is presented in the experiments shown in Figure 5, where we analyze the wetting behavior of the IL on a NW when short immersions are performed under vacuum at zero bias voltage. If the spreading parameter S is positive, then a precursor film a few nm thick will form almost instantaneously along the whole NW upon first contact with an IL reservoir even at zero bias voltage.[29] However, as S depends on the interfacial tensions into play, which in turn depend on other properties such as geometry, roughness, composition, etc., spontaneous and quasi-instantaneous wetting is not always expected.[47] Measurements at zero bias voltage performed with MCNW devices (Figure 4a−c) show no evidence of liquid transfer, but the mass detection limit of these devices is above the mass corresponding to a film of a few nm in thickness spreading totally along the NWs. However, SANW devices provide suitable performance to detect the formation of a precursor film in such conditions and to estimate its extension.

Figure 5a shows an experiment performed with a SANW device consisting on a large number of iterative short immersions (Δt_i = 1 s) at zero bias voltage. The estimations of the IL mass transferred per immersion provide an almost negligible average value. However, the initial immersion results in a singularly high value of Δm_1 = 17 ag (red dot in Figure 5a). The same behavior was consistently observed with N = 32 different SANW devices, though resulting in different values of Δm_1. Figure 5b represents the values obtained for Δm_1 for all devices vs the corresponding NW tip diameter. The values of Δm_1 are in the range of 10−1000 ag, and a clear correlation with the NW tip diameter is observed. Assuming that the IL transferred in these initial immersions forms a film on the NWs, from the values of Δm_1 it is possible to estimate the film thickness for a given extension of the film. This is represented in Figure 5c. If we consider that the film covers the whole length of the NWs, then the resulting thickness would be below 0.2 nm in all cases. Given the molecular radius of the IL used in the experiments (∼0.5 nm, Supporting Information, section 1), the results are not compatible with a film spreading along the whole length of the NWs. However, a consistent result is obtained by assuming that only the NP remaining at the NW tip is covered by IL. Figure 5c also represents the estimated thickness of a film covering the NP assuming a semispherical shell shape, as a function of the NP diameter as measured from SEM images. Remarkably, the assumption of this shape results in a cancellation of the correlation with diameter and an average thickness of 3.7 nm, a value compatible with previous studies.[29] Moreover, high resolution SEM images of Si NWs taken before and after immersions at zero bias voltage show no evidence of IL transferred along the NW length (Figure 5d,e), although the contrast changes observed in the NPs at the NW tips are compatible with the presence of a thin film only in this area (Figure 5f,g).[53] Another relevant observation regards the dispersion of the mass measurements after the first immersion, which reaches values in the range of 1−10 ag for all experiments. These values are at least 1 order of magnitude above the detection limits, so that such fluctuations can be attributed to extremely small mass exchanges between the liquid film at the NW tip and the reservoir, rather than to frequency noise. The observed selective-area wetting can be a consequence of the different composition, structure, roughness and geometry of the tip NPs with respect to the NW bodies.[65] Remarkably, the ability to detect selective-area wetting at the nanoscale demonstrates the suitability of the presented approach for fundamental studies that require extremely high resolution.

CONCLUSION

The conclusions drawn from the presented results can be summarized in three points. First, mass sensing based on resonance frequency tracking of flexural modes of beam resonators is a suitable approach in combination with voltage-driven liquid transport for precise mass flow control in open

https://doi.org/10.1021/acsnano.3c04020
ACS Nano 2023, 17, 21044−21055

nanofluidics, particularly when liquid transport remains constrained at the free end of the resonators, which implies a simplified determination of mass flow from resonance frequency shifts. Our results demonstrate this approach in such simplified condition for the sake of clarity, but this is not a fundamental limitation. The simultaneous tracking of multiple order and degenerated flexural modes can be used to obtain information about the position or extension of added mass on the resonators.[73−75] Second, the presented integration approach is scalable: NW open channels can be assembled on larger microcantilever resonators or used as resonators themselves, depending on the targeted liquid volume to be handled or on the required detection limit. The dimensions of the microcantilever resonators and/or the NWs can be also customized for the same purpose. The lowest measured mass detection limit of the NW resonators used in this work, in the order of 0.15 ag, implies the capability of handling liquid volumes below 1 zeptoliter. The largest volumes accumulated in NW channels reach to 100 femtoliters, which translates into a range of 8 orders of magnitude of volume handling capability. Finally, the scalability of the approach and the different operation modes made available suggest a wide variety of possible applications. In particular, MCNW devices operated in accumulation mode would allow to transfer/exchange/mix relatively large amounts of liquids controlled with extremely high precision between closely spaced separate locations of patterned substrates, array nanoassays or chemically functionalized lab-on-a-chip devices. The combination of liquids by sequential immersions in different reservoirs in either mode could be applied to study chemical reactions between extremely reduced volumes of reagents with external access to the liquids to trigger/stop the reactions. Also, other methodologies not limited to these modes might enable highly localized and precise interactions with bioanalytes and biointerfaces, including, for instance, fluid delivery/retrieval from single biological entities, biochemical reactions localized at specific points on their surfaces, or transfer/extraction/tracking of analytes (nanoparticles, biomolecules). We envision the specific application of our approach for nanomechanical mass sensing of nanoscaled analytes in liquids, analogously to previous approaches based on suspended microchannel resonators,[39,40] but at a largely reduced scale and with the advantage of physical access to the liquid flow for analysis or actuation. Regarding fundamental studies about the behavior of liquids at the nanoscale, further research based on SANW devices at nonzero biasing for both polarities can provide otherwise inaccessible knowledge about electrowetting and electrochemical properties of ILs.

METHODS

Silicon Nanowire Growth. Si NWs were synthesized in an atmospheric pressure chemical vapor deposition (AP-CVD) system "CVD Cube" from Nanoinnova Technologies SL. Colloidal Au NPs (Sigma-Aldrich) with nominal diameters of either 150 or 250 nm were used as growth catalyst. Before NP deposition, substrates were thoroughly cleaned in ultrasound (sequential 10 min immersions in acetone, isopropyl alcohol, and D.I. water). Next, for removing organic contaminants, the substrates were treated (1 h) with UV-ozone (Novascan) followed by immersion (10 min) in piranha solution (H_2SO_4/H_2O_2, 2:1) and then HF (5%) treated to remove native oxide (10 s immersion). Substrates were later coated by immersion (60 s) in poly-L-lysine (Sigma-Aldrich) to improve NP adhesion. Au NPs were also deposited by full immersion (30 s) of substrates into colloidal suspension (1.8×10^8 nanoparticles/mL). Si NWs were grown at a temperature of 825 °C in the tubular quartz reactor of the AP-CVD. Liquid $SiCl_4$ (Sigma-Aldrich) was used as precursor by making 30 sccm of inert Ar gas flow through a bubbler kept at a constant temperature of 0 °C. H_2 was introduced (10% in Argon) with a flow rate of 120 sccm. Growth time was 35−40 min. Tapering was controlled by introducing an auxiliary substrate coated with 20 times higher Au NP concentration and placed in an upstream position with respect to the growth substrates in the reactor tube. This extra Au supply partially compensates Au losses in the NWs during growth, modulating the resulting NW cross-section tapering. Precursor gases are purged from the reactor tube for 5 min after growth.

MCNW Device Fabrication. Silicon microcantilevers were custom fabricated by Micromotive GmbH according to author's specifications and based on their Octosensis Microcantilever-Array chips. Si NWs were made to grow horizontally at the free end of the MCs in parallel to their longitudinal axis. As Si NWs grow along (111) crystallographic directions, the parallel orientation of the NWs with respect to the longitudinal axis of the MCs is achieved by custom fabrication of the MCs with a (110) crystal orientation of their surface and a (111) orientation of their longitudinal axis. 5 in. SOI wafers with (110) device layer orientation (Si-Mat) were used for that purpose. The initial concentration of the Au NPs was adjusted in order to obtain no more than one single NW at the MC front edge. The exact position of the NW at the MC edge is not critical for the purpose of this work, which simplifies fabrication and justifies random Au NP deposition, although precise horizontal growth control is possible if specifically needed.[57]

SANW Device Fabrication. Si NWs were grown on raw Si (111) substrates without any previous patterning or fabrication steps on the substrates, except for the cleaning and Au NP deposition described above. Au NP deposition was controlled in this case by nanopipetting (Femtotip, Eppendorf) in order to ensure a minimum separation among NWs that allows signal readout from a single NW at a time, also preventing immersion of more than one NW into the IL reservoir droplet during experiments.

MCNW Device Readout. Optical readout of MCNW devices was performed by laser beam deflection transduction,[63] followed by lock-in amplification and phase lock loop monitorization (Zurich Instruments Ltd.) of the fundamental flexural mode resonance frequency of the MC. The laser beam (Schäfter + Kirchhoff GmbH, λ = 658 nm) is focused near the free end of the MC into a 4 μm diameter spot with an optical power of 40 μW. The reflected beam is collected by an unsegmented amplified photodetector (Thorlabs GmbH) in "knife-edge" configuration after being focused by a 10× objective (Mitutoyo). The signal from the photodetector is delivered to the input channel of the lock-in amplifier, whose reference signal is sent to a piezoelectric actuator (PI Ceramic GmbH) placed under the device for flexural mode excitation.

SANW Device Readout. Optical readout of SANW devices was performed by laser beam scattering modulation with transversal incidence[59] and frequency tracking based on band excitation and fast Fourier transform. The laser beam (TopMode-633, Toptica Photonics AG, λ = 633 nm) is focused by a 10× objective (Mitutoyo) into a 6 μm diameter spot with an optical power of 5 μW. The backscattered beam is collected by an unsegmented amplified photodetector (FEMTO Messtechnik GmbH), whose output signal is acquired by a DAQ board (National Instruments) and Fourier transformed into frequency spectrum by a computer. The DAQ board is synchronized with a waveform generator (Keysight Technologies) that sends a band excitation to the piezoelectric actuator (PI Ceramic GmbH) placed under the device. The center of the frequency band is defined by the tracked flexural mode resonance and its width is configured to be slightly larger than the expected frequency jumps after each liquid transfer step. The RMS amplitude of the acquired spectrum in such band is fitted to the frequency response of a linear damped harmonic oscillator in order to determine and track the resonance frequency.

Data Analysis for Determination of Mass Flow Control Range. The range of operation of mass flow control obtained with

https://doi.org/10.1021/acsnano.3c04020
ACS Nano 2023, 17, 21044−21055

different devices is determined from the measurements of mass flow rate $\dot{m}$ vs voltage V. First, V_{MAX} is determined as the voltage value where the increasing monotonic trend of mass flow changes. Then, data is fit to a function $\dot{m} = \dot{m}_0$ for $V < V_{THR}$ and $\dot{m} = \dot{m}_0 + c(V - V_{THR})^2$ for $V_{THR} < V < V_{MAX}$, where $\dot{m}_0$, c, and V_{THR} are used as fitting parameters. In cases where the mass measurements for $V < V_{THR}$ are below the mass detection limit δm, $\dot{m}_0$ is fixed to the value $\dot{m}_0 = \frac{\delta m}{\Delta t_i}$, and all values of $\dot{m} > \dot{m}_0$ for $V < V_{MAX}$ are used for the fitting to the quadratic expression above; then, V_{THR} is determined from $\dot{m}_0 = \dot{m}(V_{THR})$. For the SANW devices, the fitting is made to the whole function defined by parts, providing values to the three parameters. Finally, for both types of devices the range is given by determining the minimum and maximum mass flow rates, $\dot{m}_{MIN}$ and $\dot{m}_{MAX}$, given by $\dot{m}_{MIN} = \dot{m}(V_{THR})$ and $\dot{m}_{MAX} = \dot{m}(V_{MAX})$.

ASSOCIATED CONTENT

Supporting Information

The Supporting Information is available free of charge at https://pubs.acs.org/doi/10.1021/acsnano.3c04020.

Properties of ILs used in this work; characterization of the effective mass of the resonator devices; analysis of the accuracy of the point-mass approximation; comparison of mass measurements from nanomechanical sensing and from SEM imaging; effects of bias voltage polarity and ambient conditions on mass flow control (PDF)

AUTHOR INFORMATION

Corresponding Author

Álvaro San Paulo − *Instituto de Micro y Nanotecnología (IMN-CNM, CSIC), 28760 Tres Cantos, Madrid, Spain;* orcid.org/0000-0001-9325-8892; Phone: +34.918060709; Email: alvaro.sanpaulo@csic.es

Authors

Javier E. Escobar − *Instituto de Micro y Nanotecnología (IMN-CNM, CSIC), 28760 Tres Cantos, Madrid, Spain*

Juan Molina − *Instituto de Micro y Nanotecnología (IMN-CNM, CSIC), 28760 Tres Cantos, Madrid, Spain*

Eduardo Gil-Santos − *Instituto de Micro y Nanotecnología (IMN-CNM, CSIC), 28760 Tres Cantos, Madrid, Spain;* orcid.org/0000-0002-7100-934X

José J. Ruz − *Instituto de Micro y Nanotecnología (IMN-CNM, CSIC), 28760 Tres Cantos, Madrid, Spain;* orcid.org/0000-0003-4604-7042

Óscar Malvar − *Instituto de Micro y Nanotecnología (IMN-CNM, CSIC), 28760 Tres Cantos, Madrid, Spain;* orcid.org/0000-0001-9860-0634

Priscila M. Kosaka − *Instituto de Micro y Nanotecnología (IMN-CNM, CSIC), 28760 Tres Cantos, Madrid, Spain*

Javier Tamayo − *Instituto de Micro y Nanotecnología (IMN-CNM, CSIC), 28760 Tres Cantos, Madrid, Spain*

Montserrat Calleja − *Instituto de Micro y Nanotecnología (IMN-CNM, CSIC), 28760 Tres Cantos, Madrid, Spain;* orcid.org/0000-0003-2414-5725

Complete contact information is available at: https://pubs.acs.org/10.1021/acsnano.3c04020

Author Contributions

‡J.E.E. and J.M. contributed equally to this work. A.S.P. and M.C. conceived and designed the study. J.E.E. performed Si NW growth for all devices with contributions from J.M. for catalyst deposition for the SANW devices. J.E.E. and J.M. set up the instrumentation and performed the experiments involving MCNW and SANW devices, respectively, both with assistance from E.G.S, O.M, J.T., and P.M.K.; J.M. and A.S.P. performed the experiments within the SEM chamber. J.J.R. provided theoretical support. All authors participated in data analysis, discussed the results and contributed to the conclusions. A.S.P. wrote the manuscript with assistance from J.E.E. and J.M. and critical comments from all authors.

Notes

The authors declare no competing financial interest.

ACKNOWLEDGMENTS

This work was supported by European Research Council through ERC CoG Grant 681275; project PID2021-128395OB-I00 funded by MCIN/AEI/10.13039/501100011033/FEDER, UE; Projects PDC2022-133944-I00 and PLEC2021-007892 funded by MCIN/AEI/10.13039/501100011033 and European Union "NextGenerationEU"/PRTR; Project Y2020/BIO-65194 funded by Comunidad de Madrid; Grant RYC-2019-026626-I funded by MCIN; Project AES (DTS21/00136) funded by ISCIII/Unión Europea/FEDER. We acknowledge the service from the Micro and Nanofabrication Laboratory at IMN-CNM, funded by the Comunidad de Madrid (Project S2018/NMT-4291 TEC2-SPACE) and by MINECO (project CSIC13-4E-1794 with support from FEDER, FSE).

REFERENCES

(1) Bocquet, L. Nanofluidics Coming of Age. *Nat. Mater.* **2020**, *19* (3), 254−256.

(2) Celebi, K.; Buchheim, J.; Wyss, R. M.; Droudian, A.; Gasser, P.; Shorubalko, I.; Kye, J.-I.; Lee, C.; Park, H. G. Ultimate Permeation Across Atomically Thin Porous Graphene. *Science* **2014**, *344* (6181), 289−292.

(3) Feng, J.; Liu, K.; Graf, M.; Dumcenco, D.; Kis, A.; Di Ventra, M.; Radenovic, A. Observation of Ionic Coulomb Blockade in Nanopores. *Nat. Mater.* **2016**, *15* (8), 850−855.

(4) Feng, J.; Graf, M.; Liu, K.; Ovchinnikov, D.; Dumcenco, D.; Heiranian, M.; Nandigana, V.; Aluru, N. R.; Kis, A.; Radenovic, A. Single-Layer MoS2 Nanopores as Nanopower Generators. *Nature* **2016**, *536* (7615), 197−200.

(5) Siria, A.; Poncharal, P.; Biance, A.-L.; Fulcrand, R.; Blase, X.; Purcell, S. T.; Bocquet, L. Giant Osmotic Energy Conversion Measured in a Single Transmembrane Boron Nitride Nanotube. *Nature* **2013**, *494* (7438), 455−458.

(6) Secchi, E.; Marbach, S.; Niguès, A.; Stein, D.; Siria, A.; Bocquet, L. Massive Radius-Dependent Flow Slippage in Carbon Nanotubes. *Nature* **2016**, *537* (7619), 210−213.

(7) Tunuguntla, R. H.; Henley, R. Y.; Yao, Y.-C.; Pham, T. A.; Wanunu, M.; Noy, A. Enhanced Water Permeability and Tunable Ion Selectivity in Subnanometer Carbon Nanotube Porins. *Science* **2017**, *357* (6353), 792−796.

(8) Radha, B.; Esfandiar, A.; Wang, F. C.; Rooney, A. P.; Gopinadhan, K.; Keerthi, A.; Mishchenko, A.; Janardanan, A.; Blake, P.; Fumagalli, L.; Lozada-Hidalgo, M.; Garaj, S.; Haigh, S. J.; Grigorieva, I. V.; Wu, H. A.; Geim, A. K. Molecular Transport through Capillaries Made with Atomic-Scale Precision. *Nature* **2016**, *538* (7624), 222−225.

(9) Esfandiar, A.; Radha, B.; Wang, F. C.; Yang, Q.; Hu, S.; Garaj, S.; Nair, R. R.; Geim, A. K.; Gopinadhan, K. Size Effect in Ion Transport through Angstrom-Scale Slits. *Science* **2017**, *358* (6362), 511−513.

(10) Fumagalli, L.; Esfandiar, A.; Fabregas, R.; Hu, S.; Ares, P.; Janardanan, A.; Yang, Q.; Radha, B.; Taniguchi, T.; Watanabe, K.; Gomila, G.; Novoselov, K. S.; Geim, A. K. Anomalously Low Dielectric Constant of Confined Water. *Science* **2018**, *360* (6395), 1339−1342.

(11) Rabinowitz, J.; Cohen, C.; Shepard, K. L. An Electrically Actuated, Carbon-Nanotube-Based Biomimetic Ion Pump. *Nano Lett.* **2020**, *20* (2), 1148−1153.
(12) Abraham, J.; Vasu, K. S.; Williams, C. D.; Gopinadhan, K.; Su, Y.; Cherian, C. T.; Dix, J.; Prestat, E.; Haigh, S. J.; Grigorieva, I. V.; Carbone, P.; Geim, A. K.; Nair, R. R. Tunable Sieving of Ions Using Graphene Oxide Membranes. *Nat. Nanotechnol.* **2017**, *12* (6), 546−550.
(13) Ries, L.; Petit, E.; Michel, T.; Diogo, C. C.; Gervais, C.; Salameh, C.; Bechelany, M.; Balme, S.; Miele, P.; Onofrio, N.; Voiry, D. Enhanced Sieving from Exfoliated MoS2Membranes via Covalent Functionalization. *Nat. Mater.* **2019**, *18* (10), 1112−1117.
(14) Zhang, Z.; Wen, L.; Jiang, L. Nanofluidics for Osmotic Energy Conversion. *Nat. Rev. Mater.* **2021**, *6* (7), 622−639.
(15) Zhao, B.; Moore, J. S.; Beebe, D. J. Surface-Directed Liquid Flow Inside Microchannels. *Science* **2001**, *291* (5506), 1023−1026.
(16) Kaigala, G. V.; Lovchik, R. D.; Delamarche, E. Microfluidics in the "Open Space" for Performing Localized Chemistry on Biological Interfaces. *Angew. Chem., Int. Ed.* **2012**, *51* (45), 11224−11240.
(17) Berthier, E.; Dostie, A. M.; Lee, U. N.; Berthier, J.; Theberge, A. B. Open Microfluidic Capillary Systems. *Anal. Chem.* **2019**, *91* (14), 8739−8750.
(18) Ju, J.; Zheng, Y.; Jiang, L. Bioinspired One-Dimensional Materials for Directional Liquid Transport. *Acc. Chem. Res.* **2014**, *47* (8), 2342−2352.
(19) Si, Y.; Dong, Z. Bioinspired Smart Liquid Directional Transport Control. *Langmuir* **2020**, *36* (3), 667−681.
(20) Berthier, J.; Brakke, K. A.; Berthier, E. A General Condition for Spontaneous Capillary Flow in Uniform Cross-Section Microchannels. *Microfluid. Nanofluidics* **2014**, *16* (4), 779−785.
(21) Lee, J. J.; Berthier, J.; Theberge, A. B.; Berthier, E. Capillary Flow in Open Microgrooves: Bifurcations and Networks. *Langmuir* **2019**, *35* (32), 10667−10675.
(22) Casavant, B. P.; Berthier, E.; Theberge, A. B.; Berthier, J.; Montanez-Sauri, S. I.; Bischel, L. L.; Brakke, K.; Hedman, C. J.; Bushman, W.; Keller, N. P.; Beebe, D. J. Suspended Microfluidics. *Proc. Natl. Acad. Sci. U. S. A.* **2013**, *110* (25), 10111−10116.
(23) Berry, S. B.; Zhang, T.; Day, J. H.; Su, X.; Wilson, I. Z.; Berthier, E.; Theberge, A. B. Upgrading Well Plates Using Open Microfluidic Patterning. *Lab. Chip* **2017**, *17* (24), 4253−4264.
(24) Lee, Y.; Choi, J. W.; Yu, J.; Park, D.; Ha, J.; Son, K.; Lee, S.; Chung, M.; Kim, H.-Y.; Jeon, N. L. Microfluidics within a Well: An Injection-Molded Plastic Array 3D Culture Platform. *Lab. Chip* **2018**, *18* (16), 2433−2440.
(25) Li, K.; Ju, J.; Xue, Z.; Ma, J.; Feng, L.; Gao, S.; Jiang, L. Structured Cone Arrays for Continuous and Effective Collection of Micron-Sized Oil Droplets from Water. *Nat. Commun.* **2013**, *4* (1), 2276.
(26) Wang, Q.; Meng, Q.; Chen, M.; Liu, H.; Jiang, L. Bio-Inspired Multistructured Conical Copper Wires for Highly Efficient Liquid Manipulation. *ACS Nano* **2014**, *8* (9), 8757−8764.
(27) He, M.; Wang, P.; Xu, B.; Jiang, L.; Liu, H. The Flexible Conical Lamella: A Bio-Inspired Open System for the Controllable Liquid Manipulation. *Adv. Funct. Mater.* **2018**, *28* (49), 1800187.
(28) Duprat, C.; Protière, S.; Beebe, A. Y.; Stone, H. A. Wetting of Flexible Fibre Arrays. *Nature* **2012**, *482* (7386), 510−513.
(29) Huang, J. Y.; Lo, Y.-C.; Niu, J. J.; Kushima, A.; Qian, X.; Zhong, L.; Mao, S. X.; Li, J. Nanowire Liquid Pumps. *Nat. Nanotechnol.* **2013**, *8* (4), 277−281.
(30) Hwal Shin, J.; Hwee Kim, G.; Kim, I.; Jeon, H.; An, T.; Lim, G. Ionic Liquid Flow along the Carbon Nanotube with DC Electric Field. *Sci. Rep.* **2015**, *5* (1), 11799.
(31) Shin, J. H.; Kim, K.; Woo, H.; Kang, I. S.; Kang, H.-W.; Choi, W.; Lim, G. One-Directional Flow of Ionic Solutions along Fine Electrodes under an Alternating Current Electric Field. *R. Soc. Open Sci.* **2019**, *6* (2), No. 180657.
(32) Faez, S.; Lahini, Y.; Weidlich, S.; Garmann, R. F.; Wondraczek, K.; Zeisberger, M.; Schmidt, M. A.; Orrit, M.; Manoharan, V. N. Fast, Label-Free Tracking of Single Viruses and Weakly Scattering Nanoparticles in a Nanofluidic Optical Fiber. *ACS Nano* **2015**, *9* (12), 12349−12357.
(33) Oliveira, N. M.; Vilabril, S.; Oliveira, M. B.; Reis, R. L.; Mano, J. F. Recent Advances on Open Fluidic Systems for Biomedical Applications: A Review. *Mater. Sci. Eng., C* **2019**, *97*, 851−863.
(34) Cavaniol, C.; Cesar, W.; Descroix, S.; Viovy, J.-L. Flowmetering for Microfluidics. *Lab. Chip* **2022**, *22* (19), 3603−3617.
(35) Sharma, P.; Motte, J.-F.; Fournel, F.; Cross, B.; Charlaix, E.; Picard, C. A Direct Sensor to Measure Minute Liquid Flow Rates. *Nano Lett.* **2018**, *18* (9), 5726−5730.
(36) Zhang, Z.; Pan, J.; Tang, Y.; Xu, Y.; Zhang, L.; Gong, Y.; Tong, L. Optical Micro/Nanofibre Embedded Soft Film Enables Multifunctional Flow Sensing in Microfluidic Chips. *Lab. Chip* **2020**, *20* (14), 2572−2579.
(37) Ertsgaard, C. T.; Yoo, D.; Christenson, P. R.; Klemme, D. J.; Oh, S.-H. Open-Channel Microfluidics via Resonant Wireless Power Transfer. *Nat. Commun.* **2022**, *13* (1), 1869.
(38) Tang, M.; Liu, F.; Lei, J.; Ai, Z.; Hong, S.-L.; Zhang, N.; Liu, K. Simple and Convenient Microfluidic Flow Rate Measurement Based on Microbubble Image Velocimetry. *Microfluid. Nanofluidics* **2019**, *23* (11), 118.
(39) Burg, T. P.; Godin, M.; Knudsen, S. M.; Shen, W.; Carlson, G.; Foster, J. S.; Babcock, K.; Manalis, S. R. Weighing of Biomolecules, Single Cells and Single Nanoparticles in Fluid. *Nature* **2007**, *446* (7139), 1066−1069.
(40) Olcum, S.; Cermak, N.; Wasserman, S. C.; Christine, K. S.; Atsumi, H.; Payer, K. R.; Shen, W.; Lee, J.; Belcher, A. M.; Bhatia, S. N.; Manalis, S. R. Weighing Nanoparticles in Solution at the Attogram Scale. *Proc. Natl. Acad. Sci. U. S. A.* **2014**, *111* (4), 1310−1315.
(41) Martín-Pérez, A.; Ramos, D.; Gil-Santos, E.; García-López, S.; Yubero, M. L.; Kosaka, P. M.; San Paulo, Á.; Tamayo, J.; Calleja, M. Mechano-Optical Analysis of Single Cells with Transparent Microcapillary Resonators. *ACS Sens.* **2019**, *4* (12), 3325−3332.
(42) Meister, A.; Liley, M.; Brugger, J.; Pugin, R.; Heinzelmann, H. Nanodispenser for Attoliter Volume Deposition Using Atomic Force Microscopy Probes Modified by Focused-Ion-Beam Milling. *Appl. Phys. Lett.* **2004**, *85* (25), 6260−6262.
(43) He, M.; Zhou, Y.; Cui, W.; Yang, Y.; Zhang, H.; Chen, X.; Pang, W.; Duan, X. An On-Demand Femtoliter Droplet Dispensing System Based on a Gigahertz Acoustic Resonator. *Lab. Chip* **2018**, *18* (17), 2540−2546.
(44) Farmakidis, N.; Brown, K. A. Quantifying Liquid Transport and Patterning Using Atomic Force Microscopy. *Langmuir* **2017**, *33* (21), 5173−5178.
(45) Sbarra, S.; Waquier, L.; Suffit, S.; Lemaître, A.; Favero, I. Optomechanical Measurement of Single Nanodroplet Evaporation with Millisecond Time-Resolution. *Nat. Commun.* **2022**, *13* (1), 6462.
(46) Ondarçuhu, T.; Arcamone, J.; Fang, A.; Durou, H.; Dujardin, E.; Rius, G.; Pérez-Murano, F. Controlled Deposition of Nanodroplets on a Surface by Liquid Nanodispensing: Application to the Study of the Evaporation of Femtoliter Sessile Droplets. *Eur. Phys. J. Spec. Top.* **2009**, *166* (1), 15−20.
(47) Brochard-Wyart, F.; di Meglio, J.-M.; Quéré, D. Theory of the Dynamics of Spreading of Liquids on Fibers. *J. Phys. (Paris)* **1990**, *51* (4), 293−306.
(48) Hayes, R.; Warr, G. G.; Atkin, R. Structure and Nanostructure in Ionic Liquids. *Chem. Rev.* **2015**, *115* (13), 6357−6426.
(49) Fujita, K.; MacFarlane, D. R.; Forsyth, M. Protein Solubilising and Stabilising Ionic Liquids. *Chem. Commun.* **2005**, No. 38, 4804.
(50) Dupont, J.; Scholten, J. D. On the Structural and Surface Properties of Transition-Metal Nanoparticles in Ionic Liquids. *Chem. Soc. Rev.* **2010**, *39* (5), 1780.
(51) Naushad, Mu.; ALOthman, Z. A.; Khan, A. B.; Ali, M. Effect of Ionic Liquid on Activity, Stability, and Structure of Enzymes: A Review. *Int. J. Biol. Macromol.* **2012**, *51* (4), 555−560.
(52) Horike, S.; Ayano, M.; Tsuno, M.; Fukushima, T.; Koshiba, Y.; Misaki, M.; Ishida, K. Thermodynamics of Ionic Liquid Evaporation under Vacuum. *Phys. Chem. Chem. Phys.* **2018**, *20* (33), 21262−21268.

https://doi.org/10.1021/acsnano.3c04020
ACS Nano 2023, 17, 21044−21055

(53) Zarraoa, L.; González, M. U.; Paulo, Á. S. Imaging Low-Dimensional Nanostructures by Very Low Voltage Scanning Electron Microscopy: Ultra-Shallow Topography and Depth-Tunable Material Contrast. *Sci. Rep.* **2019**, *9* (1), 16263.
(54) Fernández-Regúlez, M.; Plaza, J. A.; Lora-Tamayo, E.; Paulo, A. S. Lithography Guided Horizontal Growth of Silicon Nanowires for the Fabrication of Ultrasensitive Piezoresistive Strain Gauges. *Microelectron. Eng.* **2010**, *87* (5−8), 1270−1273.
(55) Vidal-Álvarez, G.; Agustí, J.; Torres, F.; Abadal, G.; Barniol, N.; Llobet, J.; Sansa, M.; Fernández-Regúlez, M.; Pérez-Murano, F.; San Paulo, Á.; Gottlieb, O. Top-down Silicon Microcantilever with Coupled Bottom-up Silicon Nanowire for Enhanced Mass Resolution. *Nanotechnology* **2015**, *26* (14), No. 145502.
(56) Sahafi, P.; Rose, W.; Jordan, A.; Yager, B.; Piscitelli, M.; Budakian, R. Ultralow Dissipation Patterned Silicon Nanowire Arrays for Scanning Probe Microscopy. *Nano Lett.* **2020**, *20* (1), 218−223.
(57) Fernandez-Regulez, M.; Sansa, M.; Serra-Garcia, M.; Gil-Santos, E.; Tamayo, J.; Perez-Murano, F.; San Paulo, A. Horizontally Patterned Si Nanowire Growth for Nanomechanical Devices. *Nanotechnology* **2013**, *24* (9), No. 095303.
(58) Malvar, O.; Gil-Santos, E.; Ruz, J. J.; Ramos, D.; Pini, V.; Fernandez-Regulez, M.; Calleja, M.; Tamayo, J.; San Paulo, A. Tapered Silicon Nanowires for Enhanced Nanomechanical Sensing. *Appl. Phys. Lett.* **2013**, *103* (3), No. 033101.
(59) Molina, J.; Escobar, J. E.; Ramos, D.; Gil-Santos, E.; Ruz, J. J.; Tamayo, J.; San Paulo, Á.; Calleja, M. High Dynamic Range Nanowire Resonators. *Nano Lett.* **2021**, *21* (15), 6617−6624.
(60) Molina, J.; Ramos, D.; Gil-Santos, E.; Escobar, J. E.; Ruz, J. J.; Tamayo, J.; San Paulo, Á.; Calleja, M. Optical Transduction for Vertical Nanowire Resonators. *Nano Lett.* **2020**, *20* (4), 2359−2369.
(61) McEwen, A. B.; Ngo, H. L.; LeCompte, K.; Goldman, J. L. Electrochemical Properties of Imidazolium Salt Electrolytes for Electrochemical Capacitor Applications. *J. Electrochem. Soc.* **1999**, *146* (5), 1687−1695.
(62) Matsumoto, M.; Shimizu, S.; Sotoike, R.; Watanabe, M.; Iwasa, Y.; Itoh, Y.; Aida, T. Exceptionally High Electric Double Layer Capacitances of Oligomeric Ionic Liquids. *J. Am. Chem. Soc.* **2017**, *139* (45), 16072−16075.
(63) Kosaka, P. M.; Tamayo, J.; Gil-Santos, E.; Mertens, J.; Pini, V.; Martínez, N. F.; Ahumada, O.; Calleja, M. Simultaneous Imaging of the Topography and Dynamic Properties of Nanomechanical Systems by Optical Beam Deflection Microscopy. *J. Appl. Phys.* **2011**, *109* (6), No. 064315.
(64) Ekinci, K. L.; Huang, X. M. H.; Roukes, M. L. Ultrasensitive Nanoelectromechanical Mass Detection. *Appl. Phys. Lett.* **2004**, *84* (22), 4469−4471.
(65) Bonn, D.; Eggers, J.; Indekeu, J.; Meunier, J.; Rolley, E. Wetting and Spreading. *Rev. Mod. Phys.* **2009**, *81* (2), 739−805.
(66) Mugele, F.; Baret, J.-C. Electrowetting: From Basics to Applications. *J. Phys.: Condens. Matter* **2005**, *17* (28), R705−R774.
(67) Nanayakkara, Y. S.; Moon, H.; Payagala, T.; Wijeratne, A. B.; Crank, J. A.; Sharma, P. S.; Armstrong, D. W. A Fundamental Study on Electrowetting by Traditional and Multifunctional Ionic Liquids: Possible Use in Electrowetting on Dielectric-Based Microfluidic Applications. *Anal. Chem.* **2008**, *80* (20), 7690−7698.
(68) Cuadrado-Prado, S.; Domínguez-Pérez, M.; Rilo, E.; García-Garabal, S.; Segade, L.; Franjo, C.; Cabeza, O. Experimental Measurement of the Hygroscopic Grade on Eight Imidazolium Based Ionic Liquids. *Fluid Phase Equilib.* **2009**, *278* (1−2), 36−40.
(69) Francesco, F. D.; Calisi, N.; Creatini, M.; Melai, B.; Salvo, P.; Chiappe, C. Water Sorption by Anhydrous Ionic Liquids. *Green Chem.* **2011**, *13* (7), 1712.
(70) Jacquemin, J.; Husson, P.; Padua, A. A. H.; Majer, V. Density and Viscosity of Several Pure and Water-Saturated Ionic Liquids. *Green Chem.* **2006**, *8* (2), 172−180.
(71) Liu, W.; Cheng, L.; Zhang, Y.; Wang, H.; Yu, M. The Physical Properties of Aqueous Solution of Room-Temperature Ionic Liquids Based on Imidazolium: Database and Evaluation. *J. Mol. Liq.* **2008**, *140* (1−3), 68−72.
(72) Borghi, F.; Podestà, A. Ionic Liquids under Nanoscale Confinement. *Adv. Phys. X* **2020**, *5* (1), 1736949.
(73) Dohn, S.; Sandberg, R.; Svendsen, W.; Boisen, A. Enhanced Functionality of Cantilever Based Mass Sensors Using Higher Modes. *Appl. Phys. Lett.* **2005**, *86* (23), 233501.
(74) Gil-Santos, E.; Ramos, D.; Martínez, J.; Fernández-Regúlez, M.; García, R.; San Paulo, Á.; Calleja, M.; Tamayo, J. Nanomechanical Mass Sensing and Stiffness Spectrometry Based on Two-Dimensional Vibrations of Resonant Nanowires. *Nat. Nanotechnol.* **2010**, *5* (9), 641−645.
(75) Malvar, O.; Ruz, J. J.; Kosaka, P. M.; Domínguez, C. M.; Gil-Santos, E.; Calleja, M.; Tamayo, J. Mass and Stiffness Spectrometry of Nanoparticles and Whole Intact Bacteria by Multimode Nanomechanical Resonators. *Nat. Commun.* **2016**, *7* (1), 13452.

https://doi.org/10.1021/acsnano.3c04020
ACS Nano 2023, 17, 21044−21055